Research Article

Hunan Jiang, Jinyang Li*, Mengni Liang, Hanpeng Deng, and Zuowan Zhou*

Superior Fe_xN electrocatalyst derived from 1,1′-diacetylferrocene for oxygen reduction reaction in alkaline and acidic media

https://doi.org/10.1515/ntrev-2020-0057
received July 16, 2020; accepted July 29, 2020

Abstract: Although Fe–N/C catalysts have received increasing attention in recent years for oxygen reduction reaction (ORR), it is still challenging to precisely control the active sites during the preparation. Herein, we report Fe_xN@RGO catalysts with the size of 2–6 nm derived from the pyrolysis of graphene oxide and 1,1′-diacetylferrocene as C and Fe precursors under the NH_3/Ar atmosphere as N source. The 1,1′-diacetylferrocene transforms to Fe_3O_4 at 600°C and transforms to Fe_3N and Fe_2N at 700°C and 800°C, respectively. The as-prepared Fe_xN@RGO catalysts exhibited superior electrocatalytic activities in acidic and alkaline media compared with the commercial 10% Pt/C, in terms of electrochemical surface area, onset potential, half-wave potential, number of electrons transferred, kinetic current density, and exchange current density. In addition, the stability of FGN-8 also outperformed commercial 10% Pt/C after 10000 cycles, which demonstrates the as-prepared Fe_xN@RGO as durable and active ORR catalysts in acidic media.

Keywords: 1,1′-diacetylferrocene, RGO, ORR electrocatalyst, acidic/alkaline media

*** Corresponding author: Jinyang Li,** Key Laboratory of Advanced Technologies of Materials (Ministry of Education), School of Materials Science and Engineering, Southwest Jiaotong University, Chengdu, China, e-mail: jinyang.li@swjtu.edu.cn
*** Corresponding author: Zuowan Zhou,** Key Laboratory of Advanced Technologies of Materials (Ministry of Education), School of Materials Science and Engineering, Southwest Jiaotong University, Chengdu, China, e-mail: zwzhou@swjtu.edu.cn
Hunan Jiang, Mengni Liang, Hanpeng Deng: Key Laboratory of Advanced Technologies of Materials (Ministry of Education), School of Materials Science and Engineering, Southwest Jiaotong University, Chengdu, China

1 Introduction

Nowadays, it is of great importance to develop cleaner energy in replacement of traditional fossil energy due to the severe environmental pollution and energy crisis [1–3]. Fuel cells and metal–air batteries are regarded as promising energy conversion devices with high efficiency and little pollution [4–6]. The oxygen reduction reaction (ORR) that occurred at the cathode is usually the bottleneck due to its slow kinetics [7,8]. Currently, the most widely used ORR catalysts based on noble metals, such as Pt, Pd, etc., are still hindered by the high cost and poor cycling stability [9–11]. Therefore, the development of non-noble metal (transition metal, carbon-based) electrocatalytic materials suitable for acidic and alkaline hydrolytic materials with high activity and stability as the negative electrode of fuel and metal–air batteries has become a potential strategy [11–13].

There are many strategies for the preparation of transition metal electrocatalysts explored [14–16] since Jasinski [17] reported for the first time in 1964 that cobalt phthalocyanine exhibited oxygen reduction activity. In the realm of heterogeneous catalysis, nano-carbon materials (porous carbon, graphene, carbon nanotubes, carbon fibers) and non-metallic (N, P, S) doped nano-carbon materials are widely used as catalysts and catalyst carriers [18–20]. As the carrier of an Fe-based electrocatalyst, carbon material plays a prominent role in further inhibiting the agglomeration of nanoparticles [21], providing more catalytic active sites, and facilitating the O_2 activation [22,23]. Recently, transition metal Fe-based nanocrystals have received more and more attention as catalysts for electrocatalytic oxygen reduction [24,25]. Various iron-based compounds have been proved to be effective electrocatalysts for ORR [25], such as Fe [26], Fe_3O_4 [27], Fe_3C [28], Fe_3N [29], Fe–N–C [30], and their mixture due to the synergistic effect [27]. Some studies have shown that iron can promote the graphitization of sp^2 carbon and adjust the electronic state of the sp^2

carbon [31,32]. The graphitization of carbon is also conducive to the electron transfer of the catalyst and solidifies the nano-catalyst to reduce the agglomeration of the catalyst [25,33], and all these advantages make it have an excellent ORR activity. It has also been found that the catalytic activity of Fe-based compounds is directly related to the size of the materials [34,35]. Reducing the size of Fe-based compounds becomes a feasible solution to enhance the ORR performance [36]. Guo et al. [37] prepared a bamboo-like CNT/Fe_3C NP ORR catalyst with abundant M–N/C-active sites by the one-pot method. The catalyst exhibited a more positive half-wave potential in alkaline medium and almost the same half-wave potential in acidic electrolyte, when compared with the commercial Pt/C catalyst. Park et al. [38] wrapped graphite on nanotubes and improved the performance of the catalyst by the introduction of heteroatoms, which exhibit high catalytic activity and good stability in both acidic and alkaline media. Besides, Zhong et al. [39] introduced MOF (MIL-88B-NH_3) nanocrystals into the poly(acrylonitrile) fibers by electrospinning and created rich hierarchical pores and well-dispersed Fe_3C NPs in the catalyst, which improved its ORR catalytic performance and cycling stability in acidic electrolyte. Utilization of the electron interaction between iron and carbon carrier and adopting a reasonable design strategy, Fe_xN particles with uniform distribution and nanometer size can be prepared for broad applications in ORR electrocatalysis.

In recent years, Fe–N/C-based electrocatalysts have gradually become one of the most promising candidates for ORR. Herein, we reported an Fe–N/C catalyst (Fe_xN@rGO) prepared by a simple pyrolysis method. The large number of Fe_xN nanoparticles dispersed on the rGO support leads to rich active sites and a large surface area. According to the characterization results, the as-prepared catalysts showed premium ORR catalytic activity in both acidic and alkaline media when compared with the commercial Pt/C catalyst and rank among the top Fe_xN-based electrocatalysts, as shown in the Supporting Information (Table S1). In addition, the electrochemical surface area (ECSA) ratio of FGN-8 versus Pt/C increased from 4.33 to 7.66 after 10,000 cycles, which indicates its excellent cycling stability in an acidic electrolyte.

2 Experimental

2.1 Preparation of Fc@RGO composites

The synthesis process of Fe_xN@rGO composites is illustrated in Figure 1. Reduced graphene oxide (RGO) supported Fe_xN nanoparticles were prepared by pyrolysis of the mixed precursors. Typically, 200 mg of GO powder and 40 mg of 1,1′-diacetylferrocene (Fc@GO) were ground together and mixed thoroughly. Subsequently, the mixture was heated to 400°C for 1 h decomposition in a mix of NH_3 and Ar atmosphere (NH_3/Ar) at a heating rate of 10°C min^{-1} and then subjected to thermal annealing at 600, 700, and 800°C for 1 h, which leads to the RGO-supported Fe_xN and Fe_xO nanoparticles. Finally, the product was immersed in HCl solution (1 mol L^{-1}) at 60°C for 12 h and named as FGN-6, FGN-7, and FGN-8, respectively. The pyrolytic product of GO without Fe precursors (GN) was also prepared in NH_3/Ar at 700°C for comparison.

2.2 Electrochemical properties

The electrochemical properties of all catalysts were tested on a CHI760E electrochemical workstation with

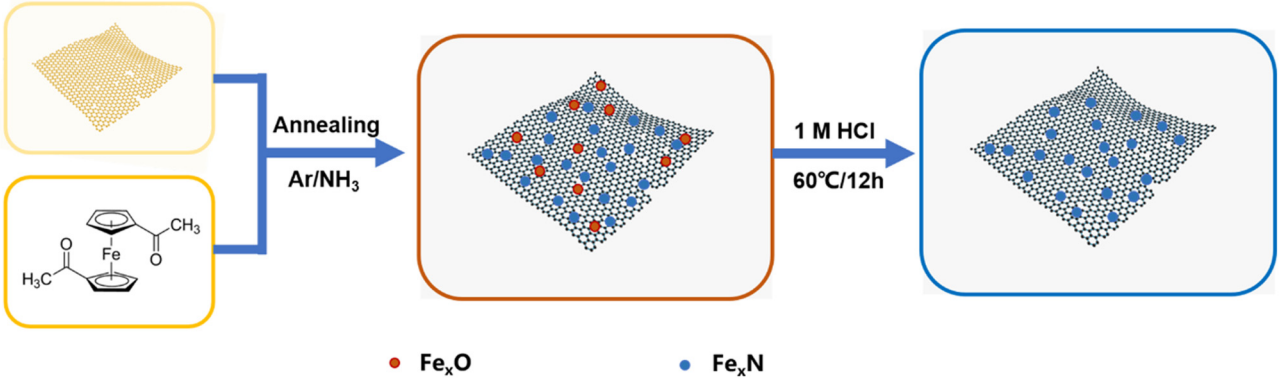

Figure 1: The schematic diagram of the synthesis process of the Fe_xN@RGO.

a typical three-electrode system. All the experimental data have been reproduced three times by using the glass carbon (5 mm) rotating disk electrode (RDE) as the working electrode carrier, Pt sheet as a counter electrode, and Hg/HgO or $Hg/HgSO_4$ as reference electrodes. The working electrode was prepared as follows: 5 mg of Fe_xN@RGO or 10% of commercial Pt/C catalyst was dispersed in 400 µL of deionized (DI) water, 180 µL of isopropanol, 400 µL of ethanol, and 20 µL of 5 wt% Nafion. The mixture solution was sonicated for 30 min before measurements. Then, 10 µL of uniform ink was loaded on a polished glassy carbon electrode and dried naturally. The electrolyte was O_2-saturated 0.1 M KOH and 0.5 M H_2SO_4, and the potential has been converted to reversible hydrogen electrode (RHE), according to the calibration curve in the Supporting Information. The cyclic voltammetry (CV) was recorded between 0 and 1.0 V (vs RHE) at a scan rate of 50 mV s^{-1}, and the linear sweep voltammetry (LSV) was carried out using RDE at 5 mV s^{-1}.

2.3 Calculation of electron transfer number of catalysis

The electron transfer number of catalysis was calculated by the Koutecký–Levich equation at the electrode potentials of 0.2, 0.3, 0.4, and 0.5 V (vs RHE). According to the Koutecký–Levich equation, the slope of linear fitting was used to calculate the number of transferred electrons (n) [40,41], given by

$$\frac{1}{J} = \frac{1}{J_L} + \frac{1}{J_k} = \frac{1}{B\omega^{1/2}} + \frac{1}{J_k} \quad (1)$$

$$B = 0.62nFC_0(D_0)^{2/3}\upsilon^{-1/6} \quad (2)$$

$$J_k = nF\kappa C_0 \quad (3)$$

where J is the measured current density, J_L and J_k are the kinetic limiting current densities and diffusion limiting current densities, and B is a parameter related to the density of the diffused current. ω is the angular velocity of the disk ($\omega = 2\pi N$, N is the linear rotation speed), n is the number of transferred electrons of ORR, F is the Faraday constant, C_0 is the saturation concentration of O_2 at room temperature environment, υ is the kinematic viscosity of the electrolyte, and κ is the electron-transfer rate constant. In 0.1 M KOH solution, the values can be determined as: $C_0 = 1.2 \times 10^{-3}$ mol^{-1}, $\upsilon = 0.1$ m^2 s^{-1}, $F = 96{,}485$ C mol^{-1}, and $D_0 = 1.9 \times 10^{-5}$ cm s^{-1}.

3 Results and discussion

This study demonstrates a simple strategy to capture Fe_xO particles decomposed from 1,1′-diacetylferrocene in a high-temperature environment by a variety of oxygen-containing functional groups on the GO/RGO surface, and then to *in situ* prepare Fe_xN nanoparticles by reaction with NH_3/Ar at high temperature. The electron micromorphology of the catalysts is shown in Figure 1. Generally, RGO presents a folded, thin-layered, porous stacking structure (as shown in Figure 2a), where the microscopic interconnected porous structure can provide a good supporting matrix for nano-Fe-based compounds. GO and 1,1′-diacetylferrocene mixtures were heat-treated in NH_3/Ar at 600, 700, and 800°C (FGN-6, FGN-7, and FGN-8). As shown in Figure 2b, FGN-6 catalyst shows nanoparticles with a size of 10–30 nm anchored on the RGO matrix. It is highly possible for the Fe-containing species on the surface to be removed thoroughly during the acid leaching. Interestingly, the FGN-7 catalyst after acid leaching shows much smaller 2–6 nm nanoparticles evenly distributed on the RGO surface, as shown in Figure 2c. When the annealing temperature reaches 800°C (FGN-8), the nanoparticles grow slightly to 3–7 nm (Figure 2d).

The XRD pattern of the pyrolysis products of Fc@GO annealed in NH_3/Ar is shown in Figure 3a, in comparison with FGN-6, FGN-7, and FGN-8. All the pyrolysis products show a broad peak at around 27°, corresponding to the (002) reflections of RGO [42]. As for FGN-6, the diffraction peaks displayed at 30.1°, 35.6°, 57.3°, and 62.9° could be assigned to (220), (311), (422), and (440) planes of the cubic spinel crystal of Fe_3O_4 (JPCDS No. 19-0629) [27,43]. After raising the annealing temperature and acid leaching, FGN-7 shows only two peaks at around 41.1° and 43.2°, corresponding to the (002) and (111) reflections of Fe_3N (JPCDS No. 72-2125) [44], respectively. For the FGN-8 catalyst, several characteristic peaks at 2θ = 37.9°, 41.4°, 43.2°, and 57.1° can be observed in the XRD pattern, which corresponds to the Fe_2N (JPCD No. 89-3939), indicating that Fe_2N nanoparticles are formed during the NH_3/Ar heat-treatment [45]. Figures 3b and c show the HRTEM image of nanoparticles in FGN-6 and FGN-8, where the lattice distances of the nanoparticles are measured to be 0.44 and 0.21 nm, corresponding to the (311) facet of Fe_3O_4 [45] and the (101) facet of Fe_2N [46], consistent with the XRD pattern. These results demonstrate that the Fe_xN nanoparticles were successfully prepared in the as-prepared catalysts.

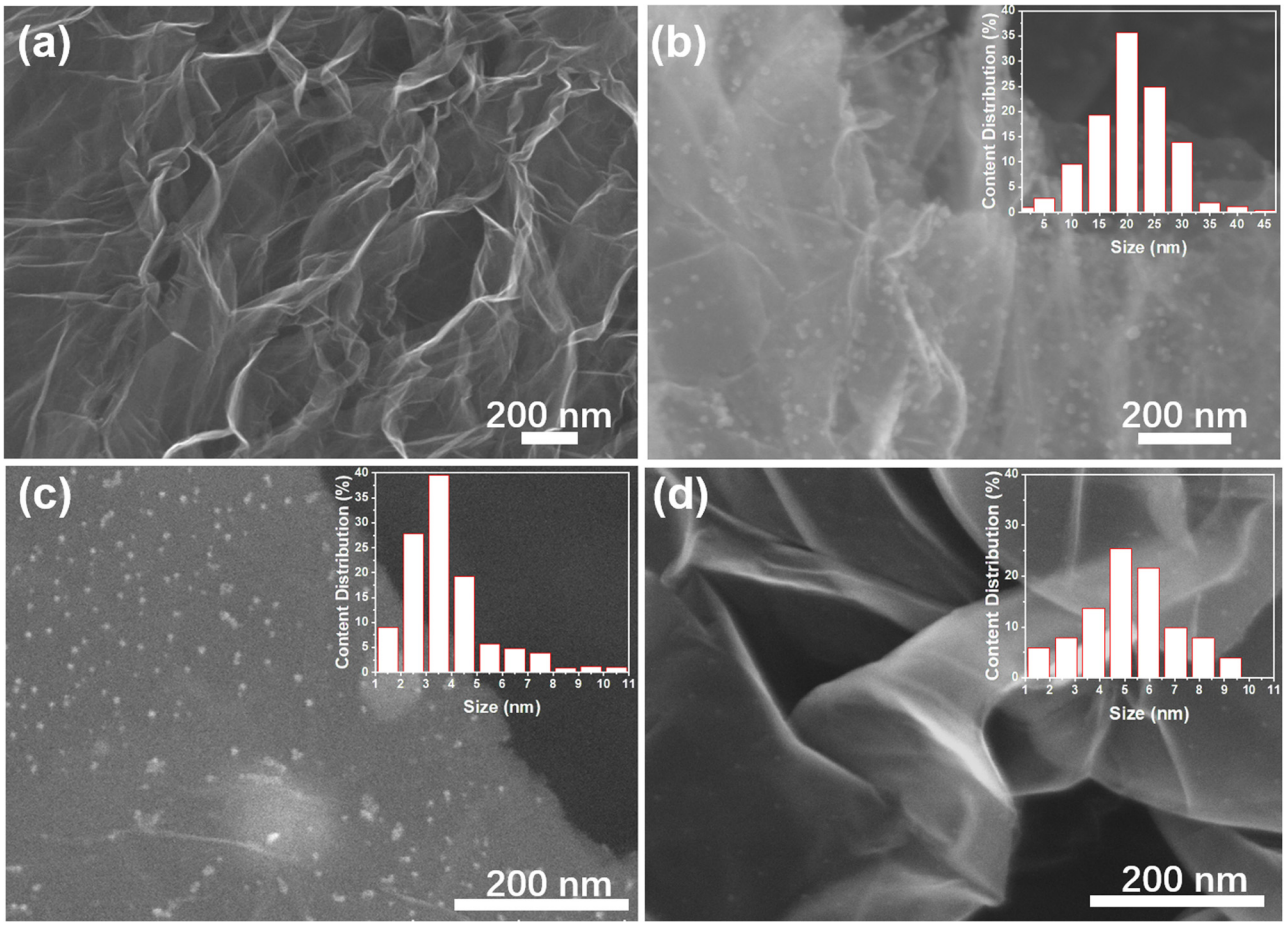

Figure 2: SEM images of (a) RGO, (b) FGN-6, (c) FGN-7, and (d) FGN-8.

Figure 3d shows the chemical composition and the corresponding bonding configurations of FGN-6, FGN-7, and FGN-8. All the electrocatalysts possess the characteristic spectra of C 1s (284.6 eV), O 1s (532.4 eV), N 1s (398–404 eV), Fe $2p_{3/2}$ (710–713 eV), and Fe $2p_{1/2}$ (723–726 eV), demonstrating the successful doping of N and Fe into RGO. The amounts of Fe, N content are tested to be 0.49%, 0.35%, 0.2% and 3.99%, 5.87%, 4.51% for FGN-6, FGN-7, and FGN-8, respectively. As shown in Figure 3e, the high-resolution Fe 2p XPS spectrum can be deconvoluted into five peaks: the peaks at 710.5 and 713.5 eV correspond to Fe^{2+} and Fe^{3+} $2p_{3/2}$, the peaks at 710.5 eV can be assigned to the coordination of Fe–N species, and the peaks at 723.5 and 726.1 eV correspond to Fe^{2+} and Fe^{3+} $2p_{1/2}$, respectively. The high-resolution N 1 s XPS spectrum can also be deconvoluted into five peaks, pyridinic-N (398.1 eV), pyrrolic-N (400.2 eV), graphitic-N (401.1 eV), oxidized-N (403.5 eV), and Fe–N (399.1 eV), as shown in Figure 3f. FGN-7 has the most notable Fe–N peak and FGN-8 has the most notable graphitic-N peak, which corresponds to the previous results that the increasing annealing temperature promotes the formation of Fe–N from 600°C to 700°C, and then the transformation of Fe_3N to Fe_2N from 700°C to 800°C. Actually, pyridinic-N and pyrrolic-N contribute to the formation of metal–nitrogen sites, and graphitic-N could facilitate the ORR performance [47], which forms the synergistic effect and improves the catalytic activity.

The texture properties of Fc@GO, FGN-6, FGN-7, and FGN-8 were characterized by nitrogen adsorption–desorption isotherms, as shown in Figures 4a and b. According to the IUPAC classification, all the catalysts exhibit a typical type-IV curve with a type-H4 hysteresis [48], which also indicates the existence of micropores and mesopores. The Fc@GO precursor exhibits a lower Brunauer–Emmett–Teller (BET) surface area of 3.29 $m^2 g^{-1}$. After heat-treatment in NH_3/Ar, the BET surface areas of FGN-6, FGN-7, and FGN-8 catalysts increased to 177.08, 266.21, and 369.98 $m^2 g^{-1}$, and the pore volumes calculated by the Barrett–Joyner–Halenda method are 1.31, 1.41, and 2.27 $cm^3 g^{-1}$, respectively. The

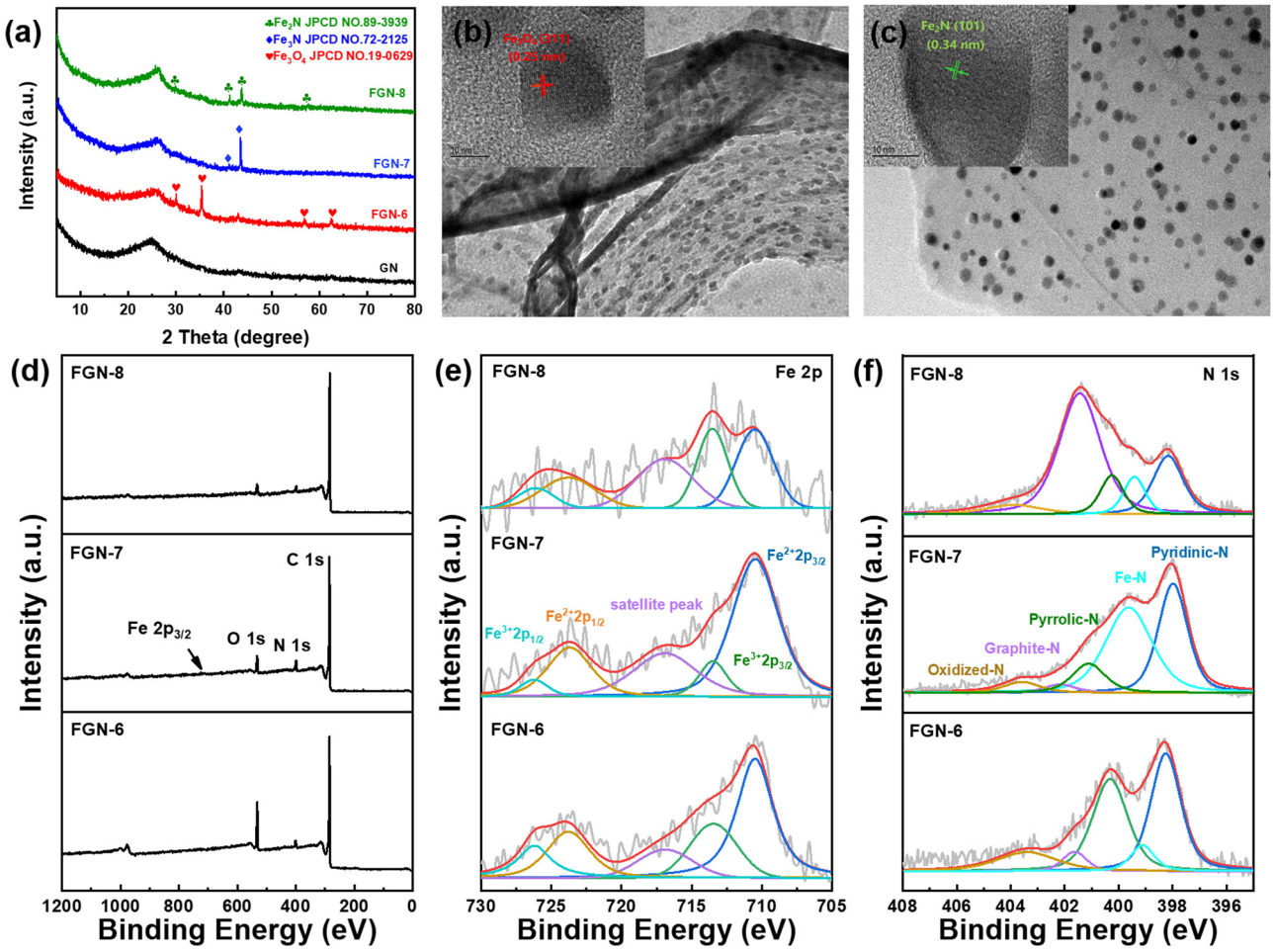

Figure 3: (a) XRD spectra of GN, FGN-6, FGN-7, and FGN-8; TEM and HRTEM of (b) FGN-6; (c) FGN-8; (d) the XPS survey spectrum, (e) Fe 2p; (f) N 1s XPS spectra of FGN-6, FGN-7, and FGN-8.

increase in surface area and pore volume can be attributed to the three-dimensional network structure formed by RGO under high temperature, and that the newly formed Fe_xN nanoparticles effectively prevent RGO nanosheets from stacking and agglomeration. Meanwhile, the higher specific surface area and larger

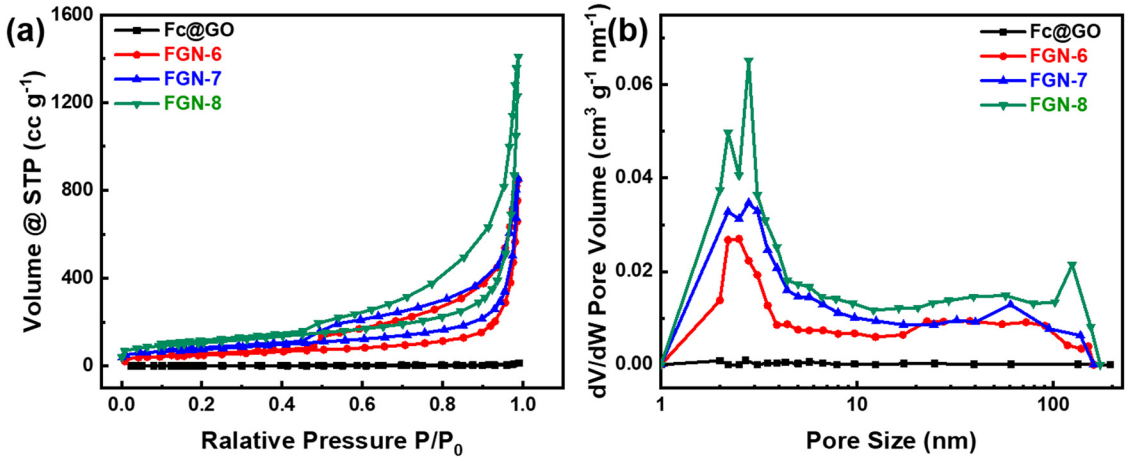

Figure 4: (a) N_2 adsorption–desorption isotherms and (b) the corresponding pore size distributions of Fc@GO, FGN-6, FGN-7 and FGN-8.

mesoporous structure can help in exposing more active sites and contributing to the diffusion of ORR-related species, hence improving the ORR activity [49].

The ORR activities of Fe_xN@RGO catalysts are first assessed by RDE in O_2-saturated 0.1 M KOH solution and compared with the commercial Pt/C (10 wt%) catalyst. The catalyst loading is 50 μg cm^{-2} and the LSV curves at different rotation speeds were measured at a potential scan rate of 5 mV s^{-1}. As shown in Figure 5a, the commercial Pt/C catalyst displays an onset (E_0) and half-wave ($E_{1/2}$) potential of 0.939 and 0.818 V (vs RHE). As shown in Figures 5b–d, the E_0 and $E_{1/2}$ of FGN-6, FGN-7, and FGN-8 are 0.844, 0.955, 0.962 and 0.729, 0.841, 0.846 V (vs RHE), respectively, which presents an excellent ORR catalytic activity. The excellent ORR activity of Fe_xN@RGO can be ascribed to the following reasons: (1) The interconnected porous structure of RGO is conducive to the loading and uniform distribution of Fe_xN nanoparticles. (2) The charge transfer between Fe_xN nanoparticles and RGO will enhance the oxygen adsorption and boost the catalytic activity of ORR [50]. (3) The evenly distributed Fe_xN nanoparticles prevent the stacking of RGO, which guarantee the high specific surface area and pore volume, strengthen the exchange interaction between oxygen and catalytic active site, and provide large electrode–electrolyte interfaces for improving the catalytic activity [51,52]. (4) Although FGN-8 has the lowest Fe content from the above XPS analysis, the successful transformation from Fe_3O_4 and Fe_2N to Fe_3N guarantees the high electrocatalytic performance.

In order to gain insights into the ORR reactive mechanism and kinetics of Fe_xN@RGO, the K–L equation was used to analyze the dynamic parameters. As shown in Figure 5a–d, the limiting current density (J_L) of catalysts increases with increasing rotation speed, that is mainly because of the increased surface flux of oxygen molecules on the catalyst and the fast electron-transfer rate at high-speed rotation [53]. Based on Figure 5a–d, the transferred electron number (n) of ORR is calculated by the K–L equation, from 0.2 to 0.5 V (vs RHE), as shown in Figure 5e–h. It can be clearly seen that the n of commercial Pt/C and FGN-8 is very close to 4.0, indicating that FGN-8 favors a four-electron ORR pathway in 0.1 M KOH. However, the n of FNG-6 is in the scope of 2.5–3.3, reflecting that the ORR of Fe_3O_4 nanoparticles is dominated by the two-electron pathway. Thus, it is not surprising to find that the n for the FGN-7 catalyst stays between 3.2 and 3.4, which indicates a mixed two-electron and four-electron pathway. Combined with the above XRD and XPS analysis, the Fe_3N nanoparticles are beneficial to increase the n of ORR.

In addition to the performance in alkaline media, the performance in acidic media is another major challenge for industrial application. In this study, the electrocatalytic activities of commercial Pt/C and FGN-8 are evaluated by LSV on RDE in O_2-saturated 0.5 M H_2SO_4 solution, with a scan rate of 5 mV/s at various rotating speeds under room temperature. As shown in Figures 6a and d, the E_0 and $E_{1/2}$ of Pt/C (0.825 and 0.656 V [vs RHE]) are much lower than those of FGN-8 (0.914 and 0.796 V [vs RHE]). Besides, the n of FGN-8 stays in the

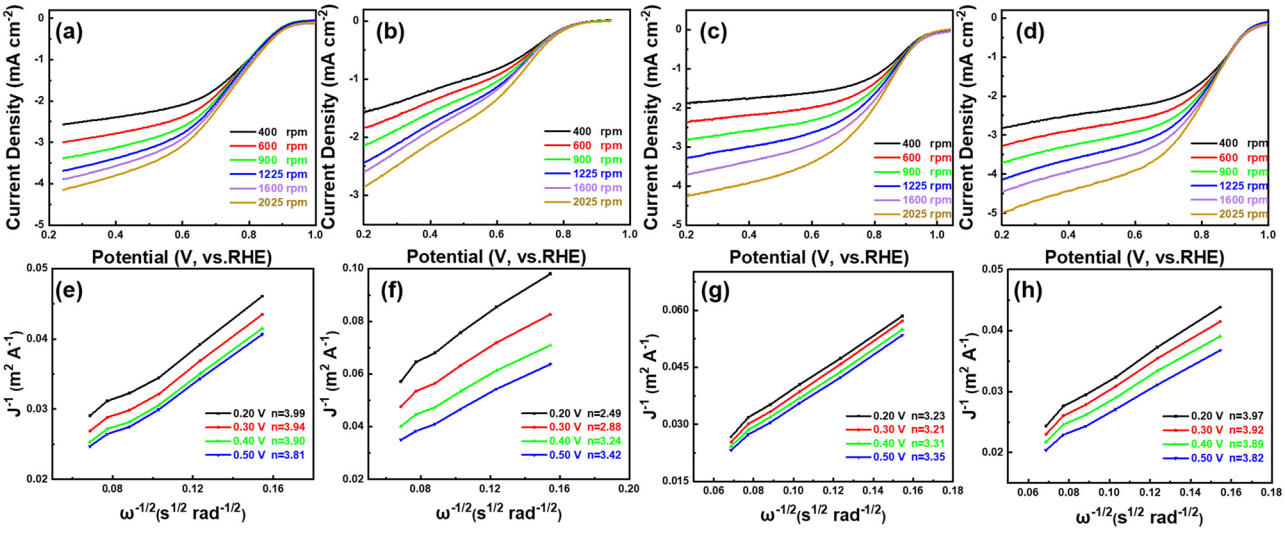

Figure 5: LSV curves with various rotation rates of (a) Pt/C, (b) FGN-6, (c) FGN-7, and (d) FGN-8. K–L plots of (e) Pt/C, (f) FGN-6, (g) FGN-7, and (h) FGN-8 from 0.2 to 0.5 V (vs RHE). All the LSV curves were tested in O_2-saturated 0.1 M KOH solution with a scan rate of 5 mV s^{-1}.

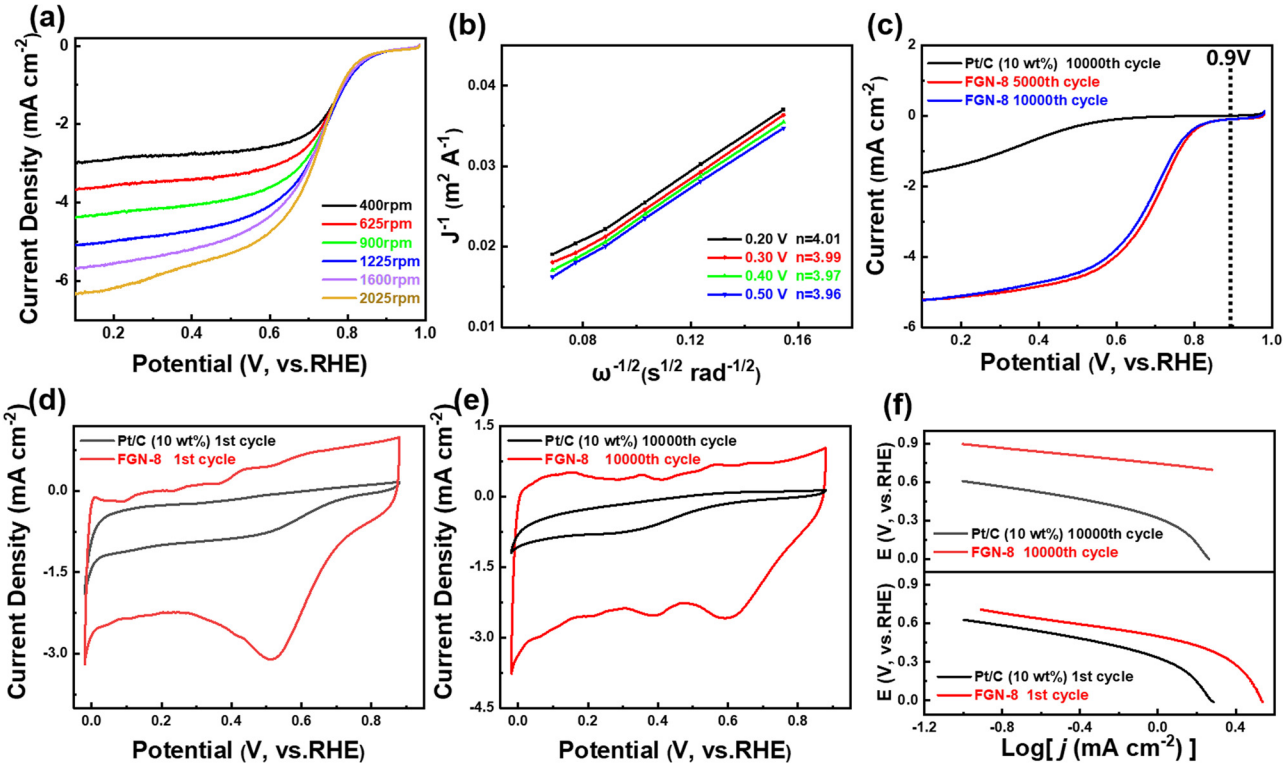

Figure 6: (a) LSV curves at different rotation rates of FGN-8. (b) K–L plots of FGN-8. (c) LSV curves of Pt/C and FGN-8 after 5,000th and 10,000th cycles. All the LSV curves were tested in O_2-saturated 0.5 M H_2SO_4 solution with a scan rate of 5 mV s^{-1} and (d and e) CV curves of commercial 10% Pt/C and FGN-8 before and after 10,000 cycles. (f) Tafel plots of Pt/C and FGN-8.

scope of 3.96–4.01, in the potential range from 0.2 to 0.5 V (vs RHE), indicating a four-electron ORR pathway in acidic media.

ECSA is another important index to evaluate the stability of catalytic activity [52,54,55]. The CV after long circulation can be used to evaluate the durability of commercial Pt/C and FGN-8 catalysts, with a scan rate of 50 mV s^{-1} in O_2-saturated 0.5 M H_2SO_4 at room temperature. In the first loop, the ECSA of FGN-8 is 4.33 times more than that of commercial Pt/C (Figure 6d). After 10,000 cycles, the ECSA ratio between FGN-8 and commercial Pt/C increased to 7.66 (Figure 6e). As shown in Figure 6c, the kinetic current densities (J_k) of the FGN-8 catalyst are 0.098 and 0.093 mA cm^{-2} at 0.9 V (vs RHE) after 5,000th and 10,000th cycles, which are almost 6.7 times that of commercial Pt/C (0.014 mA cm^{-2}). These results clearly indicate that the FGN-8 catalyst possesses a good long-term stability in acidic media.

Exchange current density (i^0) is another common parameter to evaluate the catalytic activity [53,56]. In the high potential region of 0.7–0.8 V (vs RHE), the electrode current density (i_d) is barely affected by the electrode's rotation speed, which should be the pure dynamic current density, which can be expressed as:

$$i_d = nFk_e c(O_2)\exp\{-\alpha n_\alpha F(E - E^0)/(RT)\}$$

Conversion into Tafel form:

$$E = E^0 + 2.303RT \log i^0/(\alpha n_\alpha F) - 2.303RT \log i_d/(\alpha n_\alpha F)$$

where E is the potential, E^0 is the thermodynamic potential (E^0 = 1.23 V vs RHE), F is the Faraday constant (96,487 C mol^{-1}), $c(O_2)$ is the bulk concentration of O_2 (1.2×10^{-3} mol L^{-1}), T is the temperature (298.15 K), and n_α and α are the electron transfer number and transfer coefficient of the controlled velocity step in ORR, respectively. i^0 is the exchange current density, i_d is the measured current density. E was plotted against the $\log i_d$ to obtain the Tafel curve, as shown in Figure 6f. The i^0 is calculated according to the slope ($2.303RT/(\alpha n_\alpha F)$) and the intercept ($E^0$ + 2.303RT/log $i^0/(\alpha n_\alpha F)$) of the Tafel curve. Thus, the i^0 of commercial Pt/C and FGN-8 are 3.62×10^{-7} and 6.21×10^{-7} mA/cm^2 in the first cycle, and 2.17×10^{-7} and 6.14×10^{-7} mA/cm^2 after 10,000 cycles, respectively, which proves that FGN-8 shows a better stable performance than the commercial Pt/C. Therefore, all the results manifest that FGN-8 catalyst is a suitable ORR catalyst for both acidic and alkaline media.

4 Conclusions

In summary, an excellent active Fe_xN@RGO ORR electrocatalyst both in acidic and alkaline electrolytes was developed by pyrolyzing the mixture of 1,1′-diacetylferrocene and GO in NH_3/Ar. Using the as-prepared catalyst with an average particle size of around 4 nm, and a high specific surface area with a big pore volume, the catalyst crystalline phase may derive into Fe_3N, F_2N, and N-doped RGO. Therefore, these catalysts show an excellent ORR performance in alkaline and acidic solutions. Among the above catalysts, FGN-8 shows an impressive electrocatalytic performance for ORR in 0.5 M H_2SO_4: the initial ECSA is 433% higher, the onset potential E_0 shifted 23 mV more positively, and the exchange current density i^0 is about 2 times higher. After 10,000 cycles, the ECSA is 766% higher and the J_k at 0.9 V (vs RHE) is 6.7 times higher than that of the commercial 10% Pt/C of the same loading (g cm^{-2}). This study sheds light on developing Fe_xN-based electrocatalysts for a four-electron ORR pathway in acidic and alkaline solutions, which also provide a novel strategy for the rational design of ORR catalysts with premium performance.

Acknowledgments: Funding agencies for this study include the Science and Technology Planning Project of Sichuan Province (No. 2018GZ0430, 2018GZ0135, 2018GZ0462, and 2019ZDZX0014) and the NNSF (National Natural Science Foundation of China) (No. 51772251), the Fundamental Research Funds for the Central Universities (No. 2019XJ02 and 2682020CX01), and the NBRP (National Basic Research Program) (Grant No. 2014CB931804).

Conflict of interest: The authors declare no conflict of interest regarding the publication of this paper.

References

[1] Kulkarni A, Siahrostami S, Patel A, Norskov JK. Understanding catalytic activity trends in the oxygen reduction reaction. Chem Rev. 2018;118(5):2302–12.

[2] Pegis ML, Wise CF, Martin DJ, Mayer JM. Oxygen reduction by homogeneous molecular catalysts and electrocatalysts. Chem Rev. 2018;118(5):2340–91.

[3] Li J, Doubek G, McMillon-Brown L, Taylor AD. Metallic glass nanostructures: recent advances in metallic glass nanostructures: synthesis strategies and electrocatalytic applications (Adv. Mater. 2019;7). Adv Mater. 2019;31(7):1970050.

[4] Heinzel A, Beckhaus P, Karstedt J. Membrane fuel cells. Chem Ing Technik. 2019;91(6):734–43.

[5] Gao J, Li M, Hu Y, Chen H, Ma Y. Challenges and developments of automotive fuel cell hybrid power system and control. Sci China-Information Sci. 2019;62(5):051201.

[6] Li M, Bi X, Wang R, Li Y, Jiang G, Li L, et al. Relating catalysis between fuel cell and metal-air batteries. Matter. 2020;2(1):32–49.

[7] Zhou Y, Szaro NA, Atalah J, Espina G, Blamey JM, Ramasamy RP. Electro-kinetic study of oxygen reduction reaction catalyzed by thermophilic laccase. J Electrochem Soc. 2018;165(10):H652–7.

[8] Bai B, Chen Y-T. Simulation of the oxygen reduction reaction (ORR) inside the cathode catalyst layer (CCL) of proton exchange membrane fuel cells using the Kinetic Monte Carlo Method. Energies. 2018;11(10):2529.

[9] Gu W, Hu L, Li J, Wang E. Recent advancements in transition metal-nitrogen-carbon catalysts for oxygen reduction reaction. Electroanalysis. 2018;30(7):1217–28.

[10] Duan J-J, Zheng X-X, Niu H-J, Feng J-J, Zhang Q-L, Huang H, et al. Porous dendritic PtRuPd nanospheres with enhanced catalytic activity and durability for ethylene glycol oxidation and oxygen reduction reactions. J Colloid Interface Sci. 2020;560:467–74.

[11] Cao Z, Jia J, Li H, Wang Y, Mao X, Zhang Z, et al. Fe_3C nanoparticles decorated Fe/N codoped graphene-like hierarchically carbon nanosheets for effective oxygen electrocatalysis. Int J Hydrog Energy. 2020;45(7):3930–9.

[12] Niu H-J, Zhang L, Feng J-J, Zhang Q-L, Huang H, Wang A-J. Graphene-encapsulated cobalt nanoparticles embedded in porous nitrogen-doped graphitic carbon nanosheets as efficient electrocatalysts for oxygen reduction reaction. J Colloid Interface Sci. 2019;552:744–51.

[13] Cheng W-Z, Liang J-L, Yin H-B, Wang Y-J, Yan W-F, Zhang J-N. Bifunctional iron-phtalocyanine metal-organic framework catalyst for ORR, OER and rechargeable zinc-air battery. Rare Met. 2020;39(7):815–23.

[14] Zeng K, Zheng X, Li C, Yan J, Tian J-H, Jin C, et al. Recent advances in non-noble bifunctional oxygen electrocatalysts toward large-scale production. Adv Funct Mater. 2020.

[15] Ren S, Duan X, Liang S, Zhang M, Zheng H. Bifunctional electrocatalysts for Zn-air batteries: recent developments and future perspectives. J Mater Chem A. 2020;8(13):6144–82.

[16] Zeng Z, Zhang T, Liu Y, Zhang W, Yin Z, Ji Z, et al. Magnetic field-enhanced 4-electron pathway for well-aligned Co_3O_4 /electrospun carbon nanofibers in the oxygen reduction reaction. ChemSusChem. 2018;11(3):580–8.

[17] Jasinski R. A new fuel cell cathode catalyst. Nature. 1964;201(4925):1212–3.

[18] Zhao S, Wang D-W, Amal R, Dai L. Carbon-based metal-free catalysts for key reactions involved in energy conversion and storage. Adv Mater. 2018;31:1801526.

[19] Zuo Z, Wang D, Zhang J, Lu F, Li Y. Synthesis and applications of graphdiyne-based metal-free catalysts. Adv Mater. 2018;31:1803762.

[20] Murata T, Kotsuki K, Murayama H, Tsuji R, Morita Y. Metal-free electrocatalysts for oxygen reduction reaction based on trioxotriangulene. Commun Chem. 2019;2(1):46.

[21] Ma R, Lin G, Zhou Y, Liu Q, Zhang T, Shan G, et al. A review of oxygen reduction mechanisms for metal-free carbon-based electrocatalysts. NPJ Computational Mater. 2019;5(1):78.
[22] Xie C, Niu Z, Kim D, Li M, Yang P. Surface and interface control in nanoparticle catalysis. Chem Rev. 2020;120(2):1184–249.
[23] Zhou Y, Guo Y, Li J, Wei W, Li D, Luo L, et al. Excellent antibacterial activities in the dark of ZnO nanoflakes with oxygen vacancies on exposed $\{2\bar{1}\bar{1}0\}$ facets. J Mater Chem A. 2020;8(23):11511–4.
[24] Gago AS, Habrioux A, Alonso-Vante N. Tailoring nanostructured catalysts for electrochemical energy conversion systems. Nanotechnol Rev. 2012;1(5):427–53.
[25] Dou S, Wang X, Wang S. Rational design of transition metal-based materials for highly efficient electrocatalysis. Small Methods. 2019;3(1):1800211.
[26] Wang J, Wu H, Gao D, Miao S, Wang G, Bao X. High-density iron nanoparticles encapsulated within nitrogen-doped carbon nanoshell as efficient oxygen electrocatalyst for zinc – air battery. Nano Energy. 2015;13:387–96.
[27] Gao S, Fan B, Feng R, Ye C, Wei X, Liu J, et al. N-doped-carbon-coated Fe_3O_4 from metal-organic framework as efficient electrocatalyst for ORR. Nano Energy. 2017;40:462–70.
[28] Wang M-Q, Ye C, Wang M, Li T-H, Yu Y-N, Bao S-J. Synthesis of M (Fe_3C, Co, Ni)-porous carbon frameworks as high-efficient ORR catalysts. Energy Storage Mater. 2018;11:112–7.
[29] Huang H, Gao S, Wu A-M, Cheng K, Li X-N, Gao X-X, et al. Fe_3N constrained inside C nanocages as an anode for Li-ion batteries through post-synthesis nitridation. Nano Energy. 2017;31:74–83.
[30] Wang S, Yan X, Wu K-H, Chen X, Feng J-M, Lu P, et al. A hierarchical porous Fe–N impregnated carbon-graphene hybrid for high-performance oxygen reduction reaction. Carbon. 2019;144:798–804.
[31] Wei C, Sun S, Mandler D, Wang X, Qiao SZ, Xu ZJ. Approaches for measuring the surface areas of metal oxide electrocatalysts for determining their intrinsic electrocatalytic activity. Chem Soc Rev. 2019;48(9):2518–34.
[32] Suntivich J, Gasteiger HA, Yabuuchi N, Nakanishi H, Goodenough JB, Shao-Horn Y. Design principles for oxygen-reduction activity on perovskite oxide catalysts for fuel cells and metal–air batteries. Nat Chem. 2011;3(7):546–50.
[33] Wang H, Nie S, Li H, Ali R, Fu J, Xiong H, et al. 3D hollow quasi-graphite capsules/polyaniline hybrid with a high performance for room-temperature ammonia gas sensors. ACS Sens. 2019;4(9):2343–50.
[34] Bentley CL, Kang M, Unwin PR. Nanoscale surface structure – activity in electrochemistry and electrocatalysis. J Am Chem Soc. 2018;141(6):2179–93.
[35] Majeed S, Zhao J, Zhang L, Anjum S, Liu Z, Xu G. Synthesis and electrochemical applications of nitrogen-doped carbon nanomaterials. Nanotechnol Rev. 2013;2(6):615–35.
[36] Stamenkovic V, Mun BS, Mayrhofer KJJ, Ross PN, Markovic NM, Rossmeisl J, et al. Changing the activity of electrocatalysts for oxygen reduction by tuning the surface electronic structure. Angew Chem Int Ed. 2006;45(18):2897–901.
[37] Yang W, Liu X, Yue X, Jia J, Guo S. Bamboo-like carbon nanotube/Fe_3C nanoparticle hybrids and their highly efficient catalysis for oxygen reduction. J Am Chem Soc. 2015;137(4):1436–9.
[38] Park H-S, Han S-B, Kwak D-H, Han J-H, Park K-W. Fe nanoparticles encapsulated in doped graphitic shells as high-performance and stable catalysts for oxygen reduction reaction in an acid medium. J Catal. 2019;370:130–7.
[39] Zhong R, Wu Y, Liang Z, Guo W, Zhi C, Qu C, et al. Fabricating hierarchically porous and (FeC)-C-3-embeded nitrogen-rich carbon nanofibers as exceptional electocatalysts for oxygen reduction. Carbon. 2019;142:115–22.
[40] Vondrák J. Electrochemical methods: fundamentals and applications. Surf Technol. 1983;20(1):91–2.
[41] Zhang P, Sun F, Xiang Z, Shen Z, Yun J, Cao D. ZIF-derived in situ nitrogen-doped porous carbons as efficient metal-free electrocatalysts for oxygen reduction reaction. Energy Env Sci. 2014;7(1):442–50.
[42] Schultz BJ, Dennis RV, Aldinger JP, Jaye C, Wang X, Fischer DA, et al. X-ray absorption spectroscopy studies of electronic structure recovery and nitrogen local structure upon thermal reduction of graphene oxide in an ammonia environment. RSC Adv. 2014;4(2):634–44.
[43] Guo Y, Jian X, Zhang L, Mu C, Yin L, Xie J, et al. Plasma-induced $FeSiAl@Al_2O_3@SiO_2$ core – shell structure for exceptional microwave absorption and anti-oxidation at high temperature. Chem Eng J. 2020;384:123371.
[44] Liu X, Liu H, Chen C, Zou L, Li Y, Zhang Q, et al. Fe_2N nanoparticles boosting FeNx moieties for highly efficient oxygen reduction reaction in Fe–N–C porous catalyst. Nano Res. 2019;12(7):1651–7.
[45] Zhang H-M, Zhao Y, Zhang Y, Zhang M, Cheng M, Yu J, et al. Fe_3O_4 encapsulated in porous carbon nanobowls as efficient oxygen reduction reaction catalyst for Zn–air batteries. Chem Eng J. 2019;375:122058.
[46] Liu Z, Yu J, Li X, Zhang L, Luo D, Liu X, et al. Facile synthesis of N-doped carbon layer encapsulated Fe_2N as an efficient catalyst for oxygen reduction reaction. Carbon. 2018;127:636–42.
[47] Zhang J, Sun Y, Zhu J, Kou Z, Hu P, Liu L, et al. Defect and pyridinic nitrogen engineering of carbon-based metal-free nanomaterial toward oxygen reduction. Nano Energy. 2018;52:307–14.
[48] Liu Y, Yang L, Xie B, Zhao N, Yang L, Zhan F, et al. Ultrathin Co_3O_4 nanosheet clusters anchored on nitrogen doped carbon nanotubes/3D graphene as binder-free cathodes for Al-air battery. Chem Eng J. 2020;381:122681.
[49] Shao M, Chang Q, Dodelet J-P, Chenitz R. Recent advances in electrocatalysts for oxygen reduction reaction. Chem Rev. 2016;116(6):3594–657.
[50] Hassen D, Shenashen MA, El-Safty SA, Selim MM, Isago H, Elmarakbi A, et al. Nitrogen-doped carbon-embedded TiO_2 nanofibers as promising oxygen reduction reaction electrocatalysts. J Power Sources. 2016;330:292–303.
[51] Afsahi F, Kaliaguine S. Non-precious electrocatalysts synthesized from metal – organic frameworks. J Mater Chem A. 2014;2(31):12270.
[52] Zhang Y, Shi Y, Chen R, Tao L, Xie C, Liu D, et al. Enriched nucleation sites for Pt deposition on ultrathin WO3 nanosheets with unique interactions for methanol oxidation. J Mater Chem A. 2018;6(45):23028–33.

[53] Nørskov JK, Rossmeisl J, Logadottir A, Lindqvist L, Kitchin JR, Bligaard T, et al. Origin of the overpotential for oxygen reduction at a fuel-cell cathode. J Phys Chem B. 2004;108(46):17886–92.
[54] Doña Rodríguez JM, Herrera Melián JA, Pérez Peña J. Determination of the real surface area of Pt electrodes by hydrogen adsorption using cyclic voltammetry. J Chem Educ. 2000;77(9):1195.
[55] Li Y, Xiong D, Liu Y, Liu M, Liu J, Liang C, et al. Correlation between electrochemical performance degradation and catalyst structural parameters on polymer electrolyte membrane fuel cell. Nanotechnol Rev. 2019;8(1):493–502.
[56] Seri O, Itoh Y. Differentiating polarization curve technique for determining the exchange current density of hydrogen electrode reaction. Electrochim Acta. 2016;218:345–55.